

# Film Flow in the Space between a Circular Bubble and a Square Tube<sup>1</sup>

W. BLAKE KOLB AND RAMON L. CERRO<sup>2</sup>

*Department of Chemical Engineering, The University of Tulsa, Tulsa, Oklahoma 74104-3189*

Received May 28, 1992; accepted February 12, 1993

The flow of a viscous fluid in the space defined between a bubble with circular cross section and a square tube is considered here. This problem is relevant to two-phase flows in porous media, the coating of tubes of square cross section, and more recently the design and operation of three-phase monolithic reactors. The formulation takes into account the action of gravity and the presence of a pressure field. The solution, developed as an infinite series of harmonic polynomials, satisfies the boundary conditions on the circle defined by the free-surface of the bubble and on the square defined by the wetted perimeter of the tube. The result demonstrates an efficient analytic technique for dealing with boundary conditions combining square and circular geometries. Liquid flow rates and velocity profiles measured experimentally and computed numerically agree very well with the theoretical results. © 1993 Academic Press, Inc.

## 1. INTRODUCTION

The motion of wetting liquid films in square tubes is important in multiphase flow through porous media, the coating of monolithic structures for the manufacture of catalytic converters, and, more recently, the design and operation of three-phase monolithic reactors. The wetting films arise when a wetting, viscous fluid is displaced by another immiscible fluid which may be considered inviscid, as in the case of an air bubble (1-3).

The film flow between bubbles and bubble trains and the walls of the square channels of a monolithic support have many interesting analogies with two-phase flows in porous media. In oil recovery applications, the film thickness is a measure of the fraction of oil that cannot be recovered by flooding techniques (4). Square capillaries are currently being analyzed (5-8) instead of circular because they provide a better model for describing the irregular and angular nature of porous media. In the process of coating the inside walls of the square channels of a monolithic support, the film thickness surrounding the bubble is a direct measure of the coating load (9). The main differences between the applications are in the range of flow rates and the size of the

channels. As a rule, the flow regimes of interest for flow through porous media occur at very small flow rates. The flow rates of interest in monoliths, for both the coating process and three-phase monolithic reactors, are typically much higher. The larger dimensions (millimeters versus micrometers) and vertical orientation of the square channels for monolith applications result in gravity forces which cannot be neglected.

Monolithic structures were initially developed as catalyst supports for use in automotive catalytic converters. To be useful in catalytic reactions, the monolith substrate requires that a high surface area coating be deposited upon the surface of the channel walls. The coating, which is comprised mainly of alumina and stabilizers, is used to provide a highly stable surface upon which active metals such as rhodium, platinum, and palladium are dispersed. Coating the walls of the vertically oriented monolith is usually done by forcing air through the previously liquid filled channels. When this is done, a bubble forms with the back end open—the bubble travels through the channels forcing some of the liquid out and leaving behind an annular film covering the walls. The annular wetting film deposited by an advancing bubble distributes inside the square tube in one of two configurations, as displayed in Fig. 1. These configurations were found experimentally (9) by viewing the bubble in both side (A-A) and diagonal (B-B) planes of the square tube. At low capillary numbers ( $Ca = \mu U_b / \sigma$ ), the bubble is not axisymmetric. The gas bubble flattens out against the tube walls, leaving liquid regions in the corners separated by thin flat films, as depicted in Fig. 1a. For intermediate to high  $Ca$ , an axisymmetric bubble is found (Fig. 1b). In this region the bubble radius is the same in both planes and therefore independent of  $\theta$ . The transition between these two regimes occurs at a  $Ca$  of approximately 0.1. The thickness of the deposited annular film increases with the capillary number, reaching an asymptotic maximum at large capillary numbers (9). Thus, the slower the movement of the bubble, the smaller the thickness of the film left behind. Subsequent flow of the liquid film determines whether the film will break up into liquid lenses or merely form stable liquid collars.

In recent years, the use of monolithic structures has been extended to include applications in which multiphase (gas-

<sup>1</sup> Presented at the 1989 AIChE Annual Meeting, San Francisco, CA, November 1989.

<sup>2</sup> To whom correspondence should be addressed.

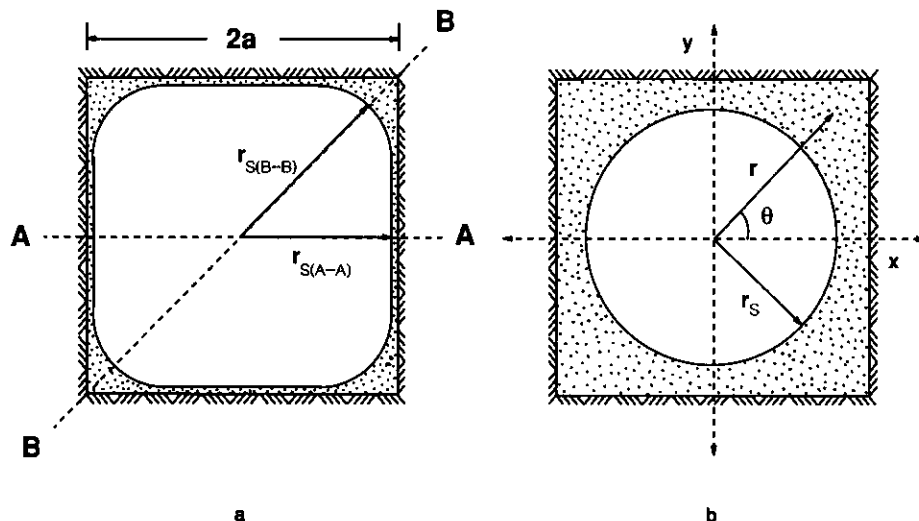


FIG. 1. Cross section of bubble inside a square tube: (a) nonaxisymmetric bubble, (b) axisymmetric bubble.

liquid) streams are processed (10–13). In these reactors, the gas and liquid are pumped into one end of the monolith and flow cocurrently in one of several flow regimes. The desired flow regime is termed slug flow. This flow regime consists of alternating gas bubbles and liquid slugs which give rise to thin film regions between the gas bubbles and channel walls and well-mixed liquid regions in the slugs. This results in enhanced mass transfer from the gas bubbles to the surface of the catalyst.

Unlike traditional packed bed reactors, the channels of the monolithic reactor have a well defined geometry and their dimensions are such that the flow regimes are always laminar. In addition, since there is no lateral mixing between the channels, each channel of the monolith essentially performs as a separate reactor. These unique properties make the monolithic reactor amenable to a detailed mathematical description once the velocity profile of the film flow around the bubble is known.

The detailed theoretical analysis of the motion of bubbles (14) and subsequent stability of the deposited annular film in square tubes relies on an analytical expression for the velocity profile in the film flowing between the bubble and the square tube walls. If one intends to back out detailed information pertaining to the flow, e.g., stagnation point location (extent of reverse flow) and transition to complete bypass flow, the velocity profile is required. We develop such a velocity profile as an infinite series solution in Section 2. In Section 3, we check the accuracy of the infinite series solution by comparing the results with those obtained from numerical simulation and experiment.

## 2. INFINITE SERIES SOLUTION

Consider the motion due to gravity of a film of viscous incompressible fluid surrounding a long inviscid cylindrical

bubble inside a tube of square cross section. Assume the axis of the tube is vertical and parallel to the gravity forces and the bubble is infinitely long. (In what follows the word “bubble” is used to describe the interface between two fluids. This term is not quite appropriate to an interface which is not closed.) Under these conditions, the flow has translational symmetry and the only nonzero component of velocity is  $(0, 0, w(x, y))$  for an  $(x, y, z)$  coordinate system. Figure 1 shows a cross section of the bubble and tube. A cylindrical coordinate system  $(r, \theta, z)$  can be defined where  $x = r \cos \theta$  and  $y = r \sin \theta$ . The width of the tube is  $2a$  and the radius of the bubble is  $r_s$ . Since the bubble is assumed infinitely long (i.e., having no ends), the pressure field can be considered constant. In dimensionless form the equations of motion are reduced to

$$\Delta W = -8. \quad [1]$$

The boundary conditions for this flow are the no-slip condition at the solid surface and the vanishing shear at the free-surface,

$$W(X, Y) = 0 \quad \text{at } X = \pm 1 \text{ and } Y = \pm 1 \quad [2a]$$

$$\frac{\partial W}{\partial R} = 0 \quad \text{at } R = R_s, \forall \theta, \quad [2b]$$

where the dimensionless variables and parameters are defined as follows:

$$R = \frac{r}{a}; X = \frac{x}{a}; Y = \frac{y}{a}.$$

$$\Delta \equiv a^2 \nabla^2; W = \frac{w}{u}; u = \frac{\rho g a^2}{8\mu}.$$

Here  $\rho$  is the fluid density,  $g$  is the acceleration due to gravity, and  $\mu$  is the coefficient of viscosity.

The characteristic velocity  $u$  is related to the average velocity for the free-surface flow of a Newtonian fluid inside a circular tube of radius  $a$ . Equations [1] and [2] define a generalized Nusselt flow; i.e., a free-surface flow where the viscous film flows on the walls of a square tube under the effect of gravity. Equation [1] will be unchanged if, instead of gravity, a constant pressure gradient is included on the right-hand side.

The solution to this problem is very simple if the boundaries have similar cross sections, i.e., both boundaries are circular or both are square. The simplest representation of the circular boundary requires a cylindrical coordinate system but the representation of a square boundary in a cylindrical system is too complicated to attempt an analytical solution. A similar situation arises if a Cartesian coordinate system is used to model the circular boundary. In Subsection 2.1, it is shown that this problem can be solved using an infinite series expansion by breaking the problem into the sum of three associated linear problems. Two of the problems are represented in a cylindrical coordinate system and the third problem in a Cartesian coordinate system. In Subsection 2.2, the combined solution to these problems is given as an infinite series expansion of harmonic functions. The harmonic functions used in the expansion have simple expressions in Cartesian as well as in cylindrical coordinate systems. The coefficients for the series expansion are computed using a collocation method on the square boundary and are discussed in Subsection 2.3.

### 2.1. Problem Formulation

The problem defined by Eqs. [1] and [2] is a linear problem and as such can be formulated as the sum of three independent linear problems,

$$W = V_1 + U + V_2, \quad [3]$$

where functions  $V_1$ ,  $U$ , and  $V_2$  are, respectively, the solutions to the following linear problems:

#### Problem I.

$$\Delta V_1(R, \theta) = -8. \quad [4]$$

$$V_1(R, \theta) = 0 \quad \text{at } R = \sqrt{2}, \forall \theta. \quad [5a]$$

$$\frac{\partial V_1}{\partial R} = 0 \quad \text{at } R = R_s, \forall \theta. \quad [5b]$$

This is a mixed-type Dirichlet-Neumann problem for the 2D Poisson equation inside the annular region defined by  $R_s \leq R \leq \sqrt{2}$ . The solution to this problem, easily obtained by integration, has cylindrical symmetry (i.e., it is not a function of  $\theta$ ), and it has a simple representation in cylindrical as well as in Cartesian coordinates,

$$V_1(R) = 2(2 - R^2) + 2R_s^2 \ln\left(\frac{R^2}{2}\right) \quad [6a]$$

$$V_1(X, Y) = 2(2 - X^2 - Y^2) + 2R_s^2 \ln\left(\frac{X^2 + Y^2}{2}\right). \quad [6b]$$

Equation [6a] was used by Reinelt (15) in the numerical solution of the flow of long bubbles inside capillaries with circular cross section.

#### Problem II.

$$\Delta U(X, Y) = 0. \quad [7]$$

$$U(X, Y) = -V_1(R, \theta) - V_2(R, \theta) \quad \text{at}$$

$$X = \pm 1 \text{ and } Y = \pm 1. \quad [8]$$

This is a Dirichlet problem for the Laplace equation inside a square. The boundary conditions, and consequently the harmonic function  $U(X, Y)$ , are unaltered by reflections on the  $X$  and  $Y$  axis and by  $\pi/2$  rotations. This is the *four corner* symmetry typical of square domains. The flow described by this equation is the parallel flow of a viscous fluid inside a square pipe with a prescribed, nonuniform velocity distribution at the walls. The boundary condition given by Eq. [8] is prescribed on a boundary of square shape.

#### Problem III.

$$\Delta V_2(R, \theta) = 0. \quad [9]$$

This is Neumann's problem for the Laplace equation in the region exterior to a circle of radius  $R_s$ . The solution to this problem is not unique, but defined up to an arbitrary constant.

$$\frac{\partial V_2}{\partial R} = -\frac{\partial U}{\partial R} \quad \text{at } R = R_s, \forall \theta. \quad [10]$$

The constant provides a degree of freedom which is used when the three problems defined in this section are combined to satisfy the boundary condition of Problem II. The harmonic function solution to Problem III has cylindrical symmetry.

It is easy to verify that the sum of the three problems described here is equivalent to the solution of the original problem (Eqs. [1] and [2]). The existing solution for Problem I and the solutions developed here for problems II and III are linearly combined to find the velocity profile in the film between a cylindrical bubble and a square tube.

### 2.2. Method of Solution

The solutions to problems II and III are infinite series expansions of harmonic polynomials. Problem II can be solved using orthogonal harmonic polynomials in the square

domain and Problem III can be solved using orthogonal harmonic polynomials in the circular domain. This approach presents two minor problems: first, polynomials that are orthogonal on the square are not orthogonal on the circular domain and vice versa; second, solutions to Problem II imply knowledge of function  $V_2$ , while solutions to Problem III demand knowledge of function  $U$ . Solving these two problems independently would require an iteration method such as Schwarz's alternating procedure (16). In order to combine the solutions of these problems, an expansion using non-orthogonal polynomials is used here. A set of orthogonal polynomials could be obtained from the set of nonorthogonal polynomials by using the Gram-Schmidt orthogonalization procedure (16). However, due to the nature of this procedure the ability to solve both problems II and III using the same set of functions would be lost.

The series expansion solution to Problems II and III is a subset of the harmonic or Laplace polynomials

$$P_m(R, \theta) = R^m \cos(m\theta) + R^{-m} \cos(m\theta) \subset z^m = R^m e^{im\theta}$$

$$\phi_m = R^m \cos(m\theta)$$

$$\psi_m = R^{-m} \cos(m\theta). \quad [11]$$

Functions  $\phi_m$  have a simple representation in Cartesian as well as in cylindrical coordinate systems. To avoid a singularity at the center,  $\psi_m$  is eliminated in the solution of Problem II. In addition, since the boundary conditions for Problem II are symmetrical with respect to reflections on the  $X$  and  $Y$  axes, only even powers of  $X$  and  $Y$  remain. Finally, since the boundary conditions are unaltered by  $\pi/2$  rotations, the expanding functions must have the four corner symmetry already discussed. Under these conditions, the only nonzero members of the set of equations defined by Eq. [11] are polynomials for which the exponents are multiples of 4; i.e.,  $m = 0, 4, 8, 12, \dots$  (17). These polynomials are orthogonal on the circle and nonorthogonal on the square and can be represented in Cartesian coordinates by the following formula (please note that  $m = 4n$ ):

$$R^{4n} \cos(4n\theta) = X^{4n} - \frac{4n!}{(4n-2)!2!} X^{4n-2} Y^2 + \frac{4n!}{(4n-4)!4!} X^{4n-4} Y^4 - \dots + Y^{4n}. \quad [12]$$

To illustrate the shape of the surface generated by these harmonic polynomials, the third member,  $\phi_8(X, Y)$ , of the sequence of polynomials defined by Eq. [12] is shown in Fig. 2 for  $m = 4n = 8$ . The three-dimensional picture of the harmonic polynomial was created using Surfer, a graphics package from Golden Software, running on an AT personal computer. In terms of  $X$  and  $Y$ ,  $\phi_8(X, Y)$  is given by

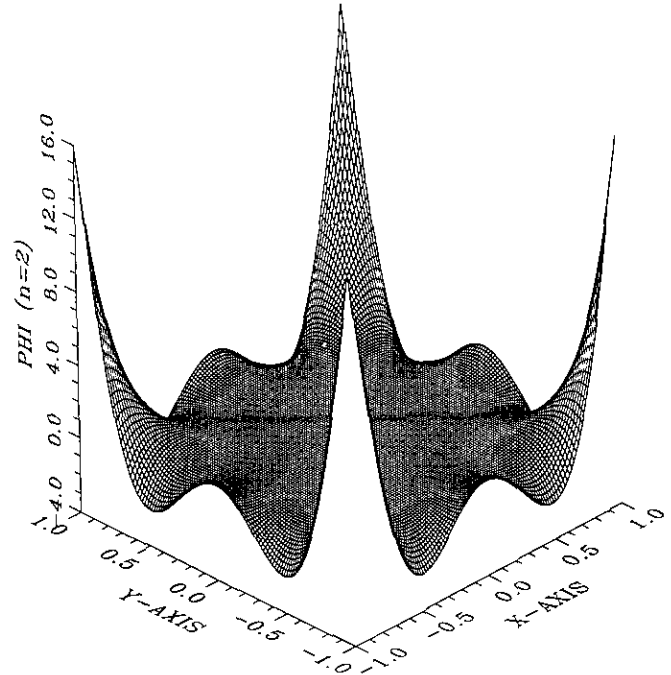


FIG. 2. Three-dimensional orthographic view of the harmonic polynomial,  $n = 2$ . The surface is symmetric with respect to  $\pi/2$  rotations.

$$\phi_8(X, Y) = X^8 - 28X^6Y^2 + 70X^4Y^4 - 28X^2Y^6 + Y^8. \quad [13]$$

The solution to Problem II can now be written as an infinite series of these harmonic polynomials,

$$U(X, Y) = \alpha_0 + \sum_{n=1}^{\infty} a_n \phi_{4n}. \quad [14]$$

Problem III is also satisfied by the harmonic polynomials defined by Eq. [11]. In this case, however,  $\phi_m$  must be eliminated to avoid an unbounded solution when  $R \rightarrow \infty$ . Note that  $\phi_m$  and  $\psi_m$  are related by

$$\psi_m(R, \theta) = \frac{\cos(m\theta)}{R^m} = \frac{\phi_m}{R^{2m}}. \quad [15]$$

In terms of  $\phi_m(R, \theta)$ , the solution to Problem III follows

$$V_2(X, Y) = \beta_0 + \sum_{n=1}^{\infty} \beta_n \frac{\phi_{4n}}{R^{8n}}. \quad [16]$$

The coefficients  $\alpha_n$  and  $\beta_n$  are computed using boundary condition [10]. By taking the partial derivatives of  $U(R, \theta)$  and  $V_2(R, \theta)$  with respect to  $R$  and evaluating the derivatives at  $R = R_s$ , the following relationship develops:

$$\sum_{n=1}^{\infty} \alpha_n \frac{\partial \phi_{4n}}{\partial R} = \sum_{n=1}^{\infty} \frac{\beta_n}{R_s^{8n}} \frac{\partial \phi_{4n}}{\partial R} \quad \text{at } R = R_s, \forall \theta. \quad [17]$$

Equation [17] is satisfied if every term of the series satisfies

$$\beta_n = \alpha_n R_s^{8n}. \quad [18]$$

Substituting Eqs. [6b], [14], [16], and [18] into Eq. [3], the expression for the velocity profile in the  $z$ -direction is obtained. This representation is given in terms of the as yet unknown coefficients  $\alpha_n$ :

$$W(X, Y) = 2(2 - X^2 - Y^2) + 2R_s^2 \ln\left(\frac{X^2 + Y^2}{2}\right) + \alpha_0 + \sum_{n=1}^{\infty} \alpha_n \left(1 + \frac{R_s^{8n}}{(X^2 + Y^2)^{4n}}\right) \phi_{4n}(X, Y). \quad [19]$$

### 2.3. Determination of Coefficients for the Series Expansion

The drawback of using nonorthogonal polynomials is the fact that the polynomials are not linearly independent and Fourier's procedure cannot be used to compute the coefficients of the series. In addition, the coefficients are not independent, and adding additional terms to the series implies computing all the coefficients again. Fortunately, the series expansion featured in Eq. [19] converges rapidly, and adding terms past the fourth term of the series does not significantly change the leading coefficients. The advantage of this method, however, is to avoid an iterative procedure to satisfy the boundary conditions. In addition, nonorthogonal polynomials are considerably simpler than their orthogonal counterparts obtained using the Gram-Schmidt procedure. This is a definite advantage when the boundary conditions (Eq. [8]) have logarithmic terms.

The remaining boundary condition at the wall of the square tube (Eq. [8]) is now used to compute the coefficients  $\alpha_n$ . A collocation procedure is used, taking advantage of the four-corner symmetry of the boundary conditions. The col-

location points are chosen on the  $Y = 1$  line for values of  $0 \leq X \leq 1$ . At every collocation point an algebraic equation relates the coefficients of the series expansion. The use of  $p$  collocation points allows the inclusion of  $p$  members of the infinite series. Five collocation points are used here at  $X = 0, 0.25, 0.5, 0.75$ , and  $1$ , allowing the determination of the coefficients for  $m = 0, 4, 8, 16$ , and  $32$ . The numerical values of these coefficients for different values of  $R_s$  are given in Table 1. These coefficients were obtained in minutes using a standard spreadsheet program in a desktop computer to solve for the system of algebraic equations defined at the collocation points.

### 2.4. Results and Discussion

Figure 3 shows three-dimensional orthographic pictures of the velocity profiles for  $R_s = 0.5, 0.7$ , and  $0.9$ . For  $m = 32$ , the solution is very accurate near the boundary since the deviations are smaller than  $0.1\%$  of the maximum velocity. For  $R_s = 0.5$ , the velocity in the corners is only slightly greater than the velocity on the sides. For  $R_s = 0.9$ , the velocity in the corners is nearly an order of magnitude greater than the velocity on the side. The graphs are not smooth for values of  $R$  smaller than  $R_s$  because the inside of the circle is not part of the solution. When the bubble radius increases, the flow in the corners becomes comparatively larger than the flow on the sides of the square. The fact that the fluid flows faster in the corners is a simple consequence of the thicker films at the corners. The flow in the corners can be used to explain some of the qualitative differences between the flow of two phases in square and in circular capillaries. This corner flow is also the reason why there are substantial differences in the flow rates when cocurrent upflow and cocurrent downflow of two fluid phases are compared (9, 14).

As was mentioned in the Introduction, the vertically oriented monolith has channel dimensions which are much larger than those found in porous media. The channels may range between  $1 \text{ mm}$  (typical of the automotive catalytic converter) and  $5 \text{ mm}$  (for some industrial reactors). For a typical fluid, this corresponds to Bond numbers ( $Bo = \rho g a^2 /$

TABLE 1

$\alpha_n R_s$	$n = 0$	$n = 1$	$n = 2$	$n = 3$	$n = 4$
0	-1.64241	-0.364895	7.74411e-3	-5.33619e-4	9.6771e-5
0.1	-1.63158	-0.361942	7.8161e-3	-5.30675e-4	9.68424e-5
0.2	-1.59908	-0.353079	8.0349e-3	-5.20399e-4	9.7279e-5
0.3	-1.54491	-0.338294	8.40478e-3	-5.01422e-4	9.82981e-5
0.4	-1.46903	-0.317518	8.94284e-3	-4.7480e-4	9.93435e-5
0.5	-1.37126	-0.29046	9.7490e-3	-4.100e-4	1.020e-4
0.6	-1.25117	-0.256345	1.10708e-2	-2.94068e-4	1.12338e-4
0.7	-1.10798	-0.21386	1.3318e-2	-3.0000e-5	1.330e-4
0.8	-0.941109	-0.16212	1.6677e-2	3.48587e-4	1.61245e-4
0.9	-0.7518	-0.10401	1.9480e-2	2.5700e-4	1.1300e-4
1.0	-0.544693	-0.0496182	1.68751e-2	-1.60671e-3	-1.56618e-4

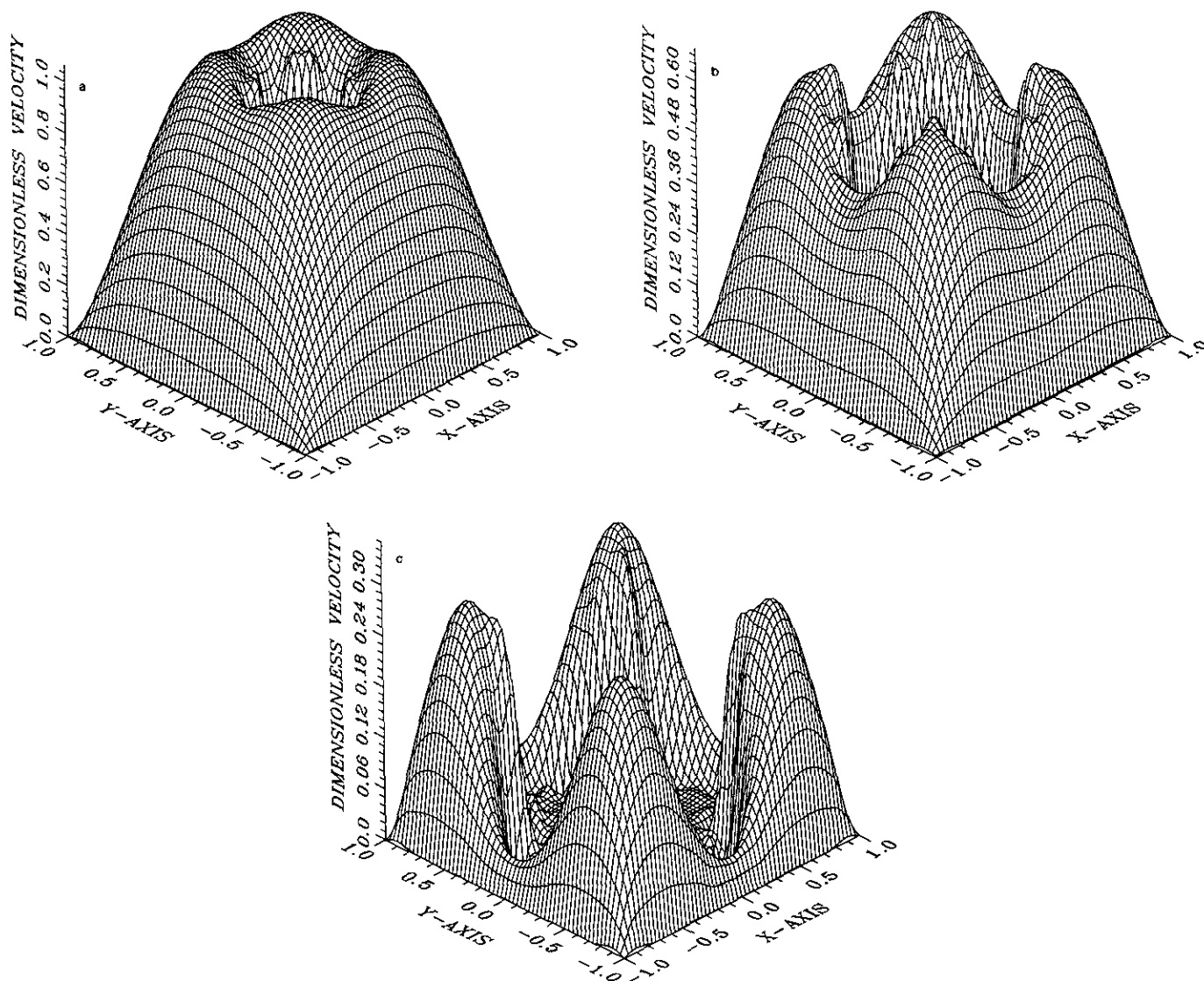


FIG. 3. Three-dimensional orthographic view of the velocity profiles in the film between a circular bubble and square tube walls for (a)  $R_s = 0.5$ , (b)  $R_s = 0.7$ , and (c)  $R_s = 0.9$ . Solution is valid only within the space defined by the circle  $R = R_s$  and the square  $-1 \leq X \leq 1$  and  $-1 \leq Y \leq 1$ .

$\sigma$ ) of approximately 0.08 and 2.0, respectively. In coating applications, the deposited film thickness or coating load (fraction of liquid left inside the channels) is the critical parameter which one would like to predict. For downflow, the flow due to gravity subtracts from the total flow into the film, thereby reducing the final film thickness. In fact, in the lower range of capillary numbers associated with coating applications, the error in predicting the final coating load (14) without inclusion of a gravity term can be as high as 30%!

Of particular interest for the three-phase monolithic reactor is the residence time distribution. Kawakami *et al.* (13) report nearly perfect mixing of the liquid phase in cocurrent upflow and plug flow for cocurrent downflow conditions. These residence time distributions point to the significance of the flow in the corner regions. Regardless of the flow di-

rection, the liquid in the corner regions moves downward under the effect of gravity. In upflow, a good degree of back-mixing occurs since the liquid in the film flows opposite the direction of the main flow. In downflow, the liquid film flows in the same direction as the main flow. As a result, the liquid phase may be considered completely mixed during upflow and essentially plug flow for downflow. Because of the mixing, the gas-liquid mass transfer coefficients are 2–5 times larger for upflow than for downflow (13).

Another application of monoliths outside the area of automotive catalytic catalysts is as a support for immobilized enzymes. Benoit and Kohler (10) evaluated the use of monoliths as a support for *catalase* in the oxidation of a citratephosphate buffer and Kawakami *et al.* (13) examined the hydrolysis and saccharification of soluble starches.

Bioengineering applications also include the use of a gel-coated monolith as a support for active organisms (18). In these applications, the adherence of the enzymes and microorganisms may be strongly dependent on the shear stresses. Figure 4 shows a three-dimensional view of the derivative of the velocity as a function of one of the coordinate directions for  $R_s = 0.7$ . The purpose of this figure is to show that the velocity field is smooth enough to be used successfully to compute shear stresses and other desirable mechanical functions.

Figure 5 shows the dimensionless flow rates,  $Q$ , as a function of  $R_s$ . The total flow rate is broken up into two parts: that within the inscribed circle and the free-surface and that in the corners. The corners account for 22% of the total area available for flow. As the radius of the bubble grows, so does the contribution of the corner flow which becomes dominant as  $R_s \rightarrow 1$ . This is attributed to the increasing percentage of the corner area available for liquid flow. An empirical equation fitting the total flow rate versus bubble radius is also included in Fig. 5. The procedure used for the integration of the velocity profiles in order to compute the flow rates is outlined in the Appendix.

### 3. COMPARISON WITH NUMERICAL AND EXPERIMENTAL RESULTS

The accuracy of the infinite series solution developed in Section 2 is examined here by comparing the results with those obtained from numerical simulation and experiment. A brief discussion of the numerical and experimental methods employed to obtain velocity profiles and flow rates is presented first.

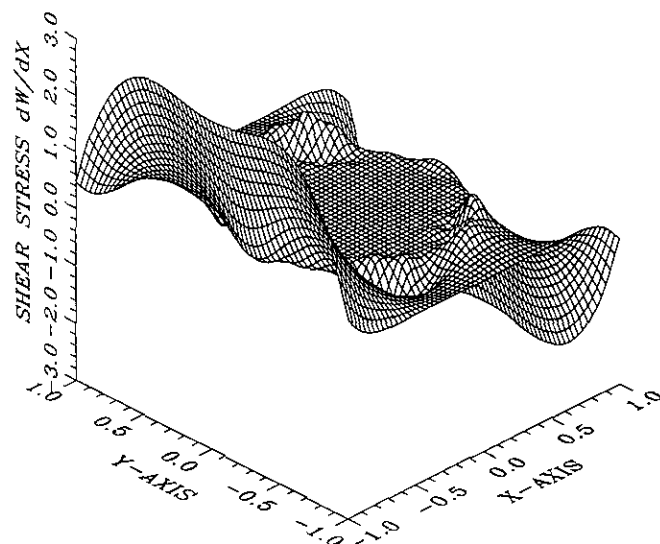


FIG. 4. Three-dimensional orthographic view of the velocity gradient,  $\partial W/\partial X$ , for  $R_s = 0.7$ .

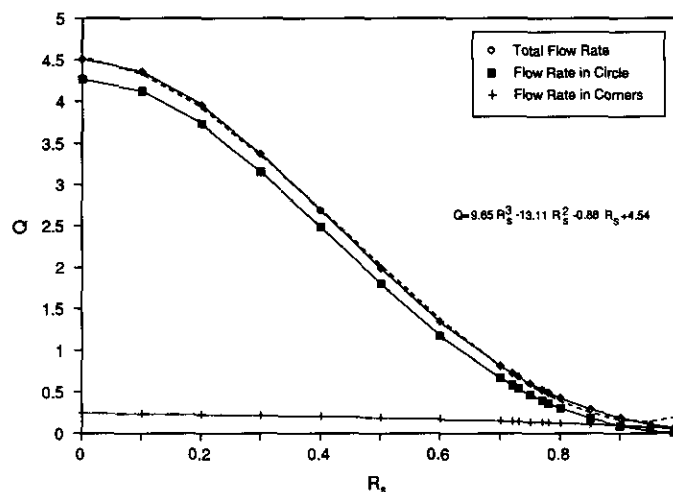


FIG. 5. Dimensionless flow rate,  $Q$ , versus dimensionless bubble radius  $R_s$ . Shown are the total flow rate, the flow rate within the inscribed circle and the free-surface, and the flow rate in the corner. The contribution of the corner flow is small for small values of  $R_s$  but becomes dominant as  $R_s \rightarrow 1$ . An empirical equation (---) for the total flow rate is also included.

#### 3.1. Numerical Procedure

The problem defined by Eqs. [1] and [2] was solved numerically with FIDAP, fluid dynamics analysis package, Version 6.0 (Fluid Dynamics International, Inc.). FIDAP is a general purpose computer program which uses the Galerkin formulation of the finite element method to simulate many classes of incompressible fluid flows. The problem is discretized in three-dimensional space using an eight node isoparametric brick element. The method of successive substitution solves the resulting linear system using direct Gaussian elimination.

#### 3.2. Experimental Procedures

In a previous study (9), we present flow visualization experiments characterizing the motion of an air bubble in an otherwise liquid filled tube. The procedure used here to deposit the film is essentially the same. The film is deposited in a vertical 30 cm long transparent square glass tube having sides of 0.30 cm (Wilma Glass Company). A pressure drop is applied across the ends of the initially silicone oil filled tube which has a metering valve and a ball valve connected in series at its exit. The ball valve serves as a "quick acting" valve to start and stop the bubble motion with minimum delay. The metering valve is used to apply an additional resistance which greatly exceeds the change in resistance due to the reduction in the liquid column as the bubble forces the liquid out. This prevents the bubble from accelerating as the tube empties and thus allows one to deposit a film of uniform thickness over as much of the tube length as possible.

Upon opening the valve an open ended bubble passes through the tube, at a velocity  $U_b$ , forcing some of the liquid

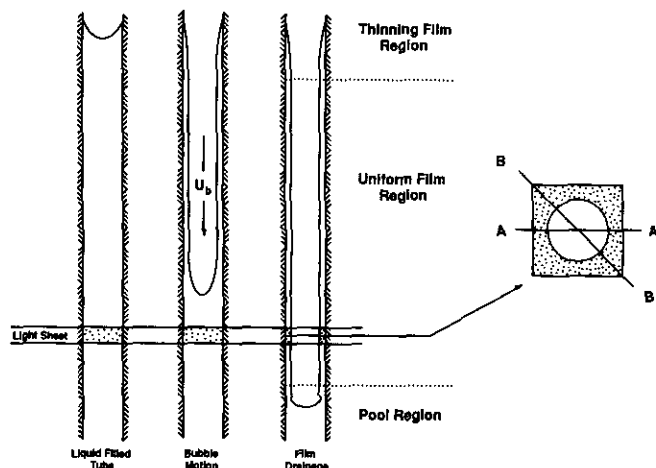


FIG. 6. The annular film deposited by an advancing bubble consisted of three regions: (1) a thinning film region, (2) a uniform film region, and (3) a pool region.

out and leaving behind an annular film of liquid on the walls, as shown in Fig. 6. The bubble is brought to rest just before it exits the tube. The resulting annular film, which drains by gravity, consists of three regions: (1) a thinning film region, (2) a uniform film region, and (3) a pool region. The thinning film region, located at the top of the tube, is a region of varying film thickness. The uniform film region is a region in which the film thickness does not change with axial position. Note that the uniform film region is always shrinking and therefore only exists for a finite period of time. Combining these two regions results in a film drainage problem analogous to that solved by Jeffreys (19) for the draining of a vertical plate. Standing waves are observed in the pool region where the annular film drains into a finite pool of liquid in the bottom of the tube. This is analogous to the back of the bubble problem presented by Bretherton (2) and the flow of a falling film into a pool presented by Rushak (20).

It is well known that thin annular films are unstable—this is no exception. Fortunately, it takes the disturbances a considerable amount of time (approximately 10 s) to grow into detectable waves. This delay provided sufficient time to measure particle velocities. The interfacial modes of instability of two-phase flows inside square tubes have been studied experimentally (Kolb and Cerro (21)).

As a model system for studying the film flow in a square tube, a 0.971 Pa·s Newtonian silicone oil (polydimethylsiloxane) was seeded with 20  $\mu$ m aluminum sphere tracer particles (Aldrich Chemical Co., Milwaukee). To perform the experiments, a sheet of light was used to illuminate a two-dimensional section tangent to the flow field in the uniform film region. The aluminum spheres seeded in the fluid scatter light as they pass through the illuminated section. A CCD camera focused on the illuminated plane was used to grab a temporal sequence of four images into the frame buffer of

microcomputer-based image capture board. The frame buffer was stored in a disk file and another sequence of four images was acquired. After several sequences were obtained, thresholding was used to separately convert each image in the temporal sequence to a binary image, a black background and a red, green, blue, or yellow foreground depending on the acquisition sequence. This produced a sequence of pseudo-colored particle tracks. The particle tracks along vertical streamlines were then determined by automatic measurement of the distances between thresholded, color-coded particles (22). This technique was used to determine the film velocity profiles in the side (A-A) and diagonal (B-B) planes of the square tube; see Fig. 6.

The reader is referred to Kolb and Cerro (9) for details of the experimental apparatus and flow visualization setup designed to study the flow in tubes of square cross section. The velocity fidelity of the flow tracer particles is an important concern for visualizing flow fields. The reader is referred to (9, 22) for details pertaining to the precautions taken to insure that the particle velocities closely matched that of the fluid.

The flow rate of the annular film was obtained experimentally by visually measuring the rise velocity of the lower meniscus in the pool region with the video system. The flow rate is calculated by multiplying the velocity of the meniscus with the known square tube cross section.

### 3.3. Results and Discussion

Selected theoretical velocity profiles for both the side and diagonal planes are compared with numerical and experimental results in Fig. 7. In this graph of  $R$  versus  $W$  the reference positions are the tube centerline at  $R = 0$ , the tube wall in the side plane at  $R = 1$ , and the tube wall in the diagonal plane at  $R = \sqrt{2}$ . The free-surface position is de-

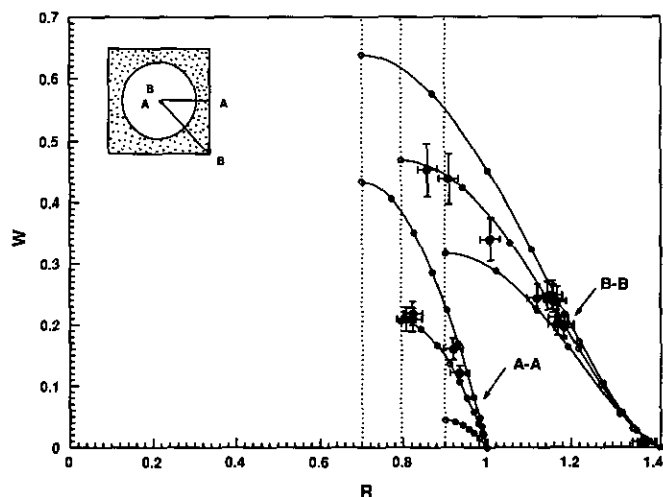


FIG. 7. Velocity profiles in side (A-A) and diagonal (B-B) planes for  $R_s = 0.7, 0.794$ , and  $0.9$ . Comparison of theoretical (—), numerical (O), and experimental results (●).



noted by the dashed line in all three cases. The infinite series solution, represented by the solid line, is compared with results obtained by the finite element method, represented by the open circles, for  $R_s = 0.7, 0.794$ , and  $0.9$ . Experimental results, represented by the solid circles, were obtained for  $R_s = 0.794$ . The accuracy of the acquired velocity data depends primarily on the adjustable search criterion (22) used by the particle tracking algorithm. This criterion, referred to as the reject criterion, was used to ensure that the distances measured represented valid particle tracks. A reject criterion of 10% was used in this work. The error in determining the particle position is estimated to be less than 2%. The reader is referred to Camp *et al.* (22) for further discussion pertaining to the accuracy of the experimental method. The velocity profiles that were measured experimentally and computed numerically are shown to agree very well with the theoretical results.

The theoretical dimensionless film flow rates are compared with those obtained from experiment in Fig. 8. The experimental results are confined to the range  $0.68 < R_s < 0.92$ . The lower limit corresponds to the asymptotic minimum value which can be achieved by the bubble motion at high capillary numbers. The upper limit corresponds to the transition in bubble symmetry, from axi- to nonaxisymmetric, which occurs at  $Ca \approx 0.1$ . The error in measuring the experimental flow rate is estimated to be less than 8%. This error results primarily from the manual, visual measurement of the lower meniscus velocity. The agreement between theory and experiment is shown to be remarkably good. The reader is referred to Kolb and Cerro (9, 14) for detailed discussions relating to these limits.

#### 4. CONCLUDING REMARKS

The flow of a viscous fluid in the space defined between a inviscid bubble with circular cross section and a square tube has been considered. The result demonstrates an efficient analytic technique for dealing with boundary conditions combining square and circular geometries.

The treatment of this problem is based on the premise that the axis of the bubble coincides with the axis of the square pipe. There is ample evidence to support this assumption as well as the fact that for large capillary numbers the bubble has a circular cross section (9). It can be argued that the pressure field generated by the movement of the front of the bubble is the factor that stabilizes the concentric bubble.

Since the harmonic polynomials are not orthogonal, the coefficients for the series expansion,  $\alpha_n$ , are not independent. To include additional terms in the series expansion, one must, in rigor, compute again all the coefficients using the collocation procedure. However, due to the fast convergence of the series, the coefficients are almost unaltered by the introduction of terms past the fourth term of the series. The

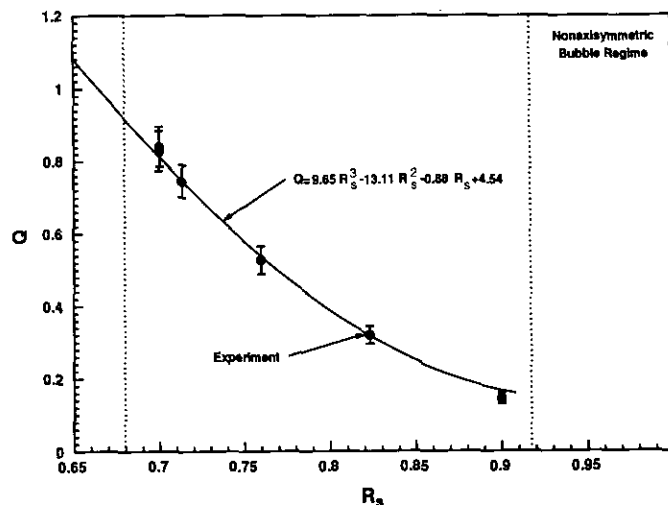


FIG. 8. Comparison of theoretical and experimental dimensionless film flow rates.

solution is only valid within the space defined by the square pipe and the circular cross section of the bubble.

#### APPENDIX

Integration of the velocity profile given by Eq. [19] in order to compute flow rates is relatively straightforward. The only complication comes from the fact that the surface domain is enclosed within a circular and a square boundary. Integration can be performed analytically using coefficients from Table 1 if the domain of integration is divided into two integrals. The first integral represents the flow across the annular surface defined between  $R = R_s$  and  $R = 1$ .

$$Q_1 = \int_0^{2\pi} \int_{R_s}^1 W(R, \theta) R dR d\theta. \quad [A1]$$

Here the flow rate is made dimensionless by  $Q = q/ua^2$ . The second integral represents the flow in the corners enclosed between the circle of unit radius and the square boundary.

$$Q_2 = \int_0^{\pi/4} \int_1^{1/\cos \theta} W(R, \theta) R dR d\theta. \quad [A2]$$

This integral is straightforward except for one term that contains  $\ln(R)$ , which results in the following integral:

$$Q_{24} = 8 \int_0^{\pi/4} \frac{\ln(\cos^2 \theta)}{\cos^2 \theta} d\theta. \quad [A3]$$

Equation [A3] was integrated using a series expansion for the logarithm. The resulting expression for the total dimensionless flow rate is given by

$$\begin{aligned}
 Q = & \frac{32}{3} - 4\pi R_s^2 + 3\pi R_s^4 - 8R_s^2 \ln 2 - 8R_s^2 \\
 & + 2.1071R_s^2 - 2\pi R_s^4 \ln\left(\frac{R_s^2}{2}\right) + \alpha_0(4 - \pi R_s^2) \\
 & - \alpha_1\left(\frac{16}{15} + \frac{R_s^8}{3}\right) + \alpha_2\left(\frac{36}{45} + \frac{R_s^{16}}{84}\right) - \alpha_3\left(\frac{256}{91} + \frac{R_s^{24}}{880}\right) \\
 & + \alpha_4\left(\frac{1024}{153} + \frac{R_s^{32}}{6720}\right) - \dots \quad [A4]
 \end{aligned}$$

### ACKNOWLEDGMENTS

The authors are grateful to Allied Signal Inc. and The Office of Research and the Associate Dean for Research of the CE&AS of The University of Tulsa for support of this research.

### REFERENCES

1. Taylor, G. I., *J. Fluid Mech.* **10**, 161 (1961).
2. Bretherton, F. P., *J. Fluid Mech.* **10**, 166 (1961).
3. Fairbrother, F., and Stubbs, A. E., *J. Chem. Soc.* **1**, 527 (1935).
4. Singhal, A. K., and Somerton, W. H., *J. Can. Pet. Technol.* **197** (1970).
5. Gauglitz, P. A., St. Laurent, C. M., and Radke, C. M., *J. Pet. Technol.* **39**, 1137 (1987).
6. Ransohoff, T. C., Gauglitz, P. A., and Radke, C. M., *AIChE J.* **33**, 753 (1987).
7. Ransohoff, T. C., and Radke, C. M., *Phys. Chem. Hydrodyn.* **8**, 255 (1987).
8. Ransohoff, T. C., and Radke, C. M., *J. Colloid Interface Sci.* **121**, 392 (1988).
9. Kolb, W. B., and Cerro, R. L., *Chem. Eng. Sci.* **46**, 2181 (1991).
10. Benoit, M. R., and Kohler, J. T., *Biotechnol. Bioeng.* **17**, 1617 (1975).
11. Satterfield, C. N., and Ozel, F., *I&EC Fundamentals* **16**, 61 (1977).
12. Irandoust, S., and Andersson, B., *Ind. Eng. Chem. Res.* **28**, 1489 (1988).
13. Kawakami, K., Kawasaki, K., Shiraishi, F., and Kusunoki, K., *Ind. Eng. Chem. Res.* **28**, 394 (1989).
14. Kolb, W. B., and Cerro, R. L., *Phys. Fluids A*, in press.
15. Rienelt, D. A., *J. Fluid Mech.* **175**, 557 (1987).
16. Courant, R., and Hilbert, D., "Methods of Mathematical Physics." Wiley-Interscience, New York, 1966.
17. Kantorovich, L. V., and Krylov, V. I., "Approximate Methods of Higher Analysis." Noordhoff, Groningen, 1964.
18. Ariga, O., Kimura, M., Taya, M., and Kobayashi, T., *Ferment Technol.* **64**, 327 (1986).
19. Jeffreys, *Proc. Cambridge Philos. Soc.* **26**, 204 (1930).
20. Rushak, K. J., *AIChE J.* **24**, 705 (1978).
21. Kolb, W. B., and Cerro, R. L., *AIChE Annual Meeting*, Paper No. 116f, Los Angeles, CA, Nov. 1991.
22. Camp, C. E., Kolb, W. B., Sublette, K. L., and Cerro, R. L., *Exp. Fluids* **10**, 87 (1990).